Available online at www.sciencedirect.com

SciVerse ScienceDirect

Ceramics International 39 (2013) 7779–7785

CERAMICS INTERNATIONAL

www.elsevier.com/locate/ceramint

Synthesis and characterization of lithium calcium phosphate ceramics

Omer Kaygili[a,*], Serhat Keser[b], Tankut Ates[a], Fahrettin Yakuphanoglu[a,c]

[a]Department of Physics, Faculty of Science, Firat University, 23119 Elazig, Turkey
[b]Department of Chemistry, Faculty of Science, Firat University, 23119 Elazig, Turkey
[c]Faculty of Science, Department of Physics, King Abdulaziz University, Jeddah 21589, Saudi Arabia

Received 7 January 2013; received in revised form 6 February 2013; accepted 12 March 2013
Available online 20 March 2013

Abstract

The crystal structure, thermal, dielectrical, alternating current conductivity and microstructure properties of lithium calcium phosphate ceramics synthesized by the sol–gel method were investigated. The average crystallite size, crystallinity, activation energy and enthalpy of crystallization of $Ca_{10}Li(PO_4)_7$ ceramics were determined. The X-ray diffraction (XRD) results indicated that the apatitic structure belonging to HAp was transformed fully to $Ca_{10}Li(PO_4)_7$ phase with the addition of Li. The Avrami exponents of the samples suggest that the crystallization mechanism is based on the surface nucleation and one-dimensional growth. It was found that the alternating current conductivity mechanism of the ceramics is controlled by the hopping motion involving a translational motion with a sudden hopping. The dielectric constant of the samples shows a small increase with increasing amount of Li.
© 2013 Elsevier Ltd and Techna Group S.r.l. All rights reserved.

Keywords: Sol–gel method; Calcium phosphates; Activation energy; Crystal structure

1. Introduction

Ceramics used in biomedical applications are named as bioceramics and, they have been extremely used in the treatment of bones, joints and teeth as implant materials since they possess a lot of desirable properties such as chemical stability and non-toxicity [1–3]. Hydroxyapatite (HAp, $Ca_{10}(PO_4)_6(OH)_2$), with a composition similar to that of the mineral phase of bone and teeth, is one of the most known bioceramics, and its crystal system is hexagonal [4–9]. HAp is both biocompatible and bioactive, as well as osteoconductive [10–13]. Sol–gel, which is one of the most preferred methods, has been used to synthesize HAp with high product purity and low synthesis temperature [14–16]. Additionally, HAp is a dielectric material and can be used in the electrical systems. The electrical and dielectrical properties of HAp are an important scientific issue due to the possible applications of HAp material in the fabrication of biological sensors. Furthermore, the electromagnetic fields have been shown to accelerate healing in bone fractures [17]. For this reason, electrical properties of HAp are very important research topic to determine physical properties, especially microstructures, because these measurements are both non-destructive and rapid [18,19].

The chemical, physical, microstructure and dielectrical properties of HAp have been improved with the addition of specific elements such as Mg, Zn, and Sr. Although Mg and Zn are most preferred and used elements as dopants for HAp, Li^+ ions are smaller than Mg^{2+} and Zn^{2+} and can pass through biological membranes and reach control sites. It is well known that lithium (Li), which is present in the human body in trace amounts, is an alkali metal and is known to be a bioelectric material [18,19]. Li, which is an inexpensive drug, has been used in hematology and psychiatry for the treatment of bipolar disorder. Moreover, the stimulating effects of Li (as lithium chloride and lithium carbonate) on proliferation of the human cells, such as thyroid and pancreatic beta cells, have been reported [20–25].

This work mainly focuses on the synthesis, structural characterization and measurements of calorimetric and physical properties of Li-containing calcium phosphate ceramic samples. The experimental results were compared with hydroxyapatite, since all the ceramic samples were synthesized using HAp (chemical formulae).

*Corresponding author. Tel.: +90 424 2370000/3623; fax: +90 424 2330062.
E-mail address: okaygili@firat.edu.tr (O. Kaygili).

0272-8842/$ - see front matter © 2013 Elsevier Ltd and Techna Group S.r.l. All rights reserved.
http://dx.doi.org/10.1016/j.ceramint.2013.03.037

2. Experimental

Lithium calcium phosphate ceramics, having the molar ratio (Ca+Li)/P equal to 1.67, were prepared with two various atomic ratios of lithium (10 and 20 at%) using the sol–gel method. The synthesis of lithium calcium phosphate ceramics was performed using $Ca(NO_3)_2{\bullet}4H_2O$, P_2O_5 and $LiNO_3$ reagents dissolved in anhydrous ethanol. The chemicals were dissolved in ethanol for about 1 h. The prepared solutions with Ca and P were poured into a beaker, and were mixed for about 15 min. Then, Li-containing solution was dropped slowly into this mixture, and vigorously stirred for about 30 min. The obtained gel was shaken into a hot-water bath at 60 °C for 2 h, and was then dried in an oven at 120 °C for 15 h. The dried samples were sintered in an electric furnace at 900 °C for 1.5 h.

X-ray diffraction (XRD) data of the samples were collected on a Bruker D8 Advance Diffractometer using Ni-filtered Cu Kα radiation produced at 40 kV and 40 mA. Differential thermal analysis (DTA) measurements of the samples were performed by a Perkin-Elmer equipment at the heating rates of 5, 10, 15 and 20 °C min^{-1} from ambient temperature to 1000 °C. The possible functional groups were detected by a Perkin-Elmer spectrophotometer in the mid-infrared region (4000–400 cm^{-1}) using the KBr pellets. A 3532-50 LCR HiTESTER was used to measure the values of impedance and capacitance in the range of 10 kHz–1 MHz frequency regions. The microstructure of the samples was studied by a scanning electron microscope (LEO EVO 40VXT) operated at 20 kV acceleration voltage.

3. Results and discussion

The crystal structure of the Li including HAp samples was characterized by X-ray diffraction spectra and XRD results of the samples are given together with those of pure HAp published in previous work [17] in Fig. 1. The average crystallite size was calculated using the Debye–Scherrer equation [26]

$$D = \frac{0.9\lambda}{\beta_{1/2}cos\theta} \quad (1)$$

where λ is the wavelength of X-rays (λ=0.15406 nm for CuKα radiation), $\beta_{1/2}$ is the full width at half maximum (FWHM) in radian and θ is the diffraction angle.

The effective crystallite size (D_{WH}) and micro-strain (ε) values were determined by the following Williamson–Hall equation [27]:

$$\frac{\beta_{1/2}cos\theta}{\lambda} = \frac{1}{D_{WH}} + \frac{\varepsilon sin\theta}{\lambda} \quad (2)$$

Furthermore, the crystalline phases in the XRD patterns of the samples were identified by means of JCPDS (Joint Committee on Powder Diffraction Standards) cards. The presence of crystalline lithium calcium phosphate ($Ca_{10}Li(PO_4)_7$, PDF No. 45-0550) phase, with trigonal crystal structure, was obtained in both samples. XRD results of the samples are in perfect harmony with those of Song et al. [28].

XRD patterns of the samples changed with different Li contents. The magnitude of crystalline peaks in the XRD spectra of the samples decreased significantly with the increase of Li content from 10 at% to 20 at%. With the incorporation of Li into HAp, β-TCP and hydroxyapatite phases disappeared and a lithium calcium phosphate ($Ca_{10}Li(PO_4)_7$ phase was formed with Li content.

The average crystallite size (D_{DS}) was found to be 34 nm for 10 at% Li and 59 nm for 20 at% Li. Also, the effective crystallite size (D_{WH}) was found to be 37 nm for 10 at% Li and 55 nm for 20 at% Li. Both Debye–Scherrer and Williamson–Hall analyses are in accordance with each other. The micro-strain (ε) values were found to be 0.041 for 10 at% Li and 0.096 nm for 20 at% Li, and this parameter was increased about two times with the addition of Li. However, this considerable micro-strain has not been found in other works.

The crystallinity (X_C) can be estimated by the following relation [18]:

$$X_C = \frac{\sum A_C}{\sum A_C + \sum A_A} \quad (3)$$

where $\sum A_C$ is the total area under crystal peaks, and $\sum A_A$ is the total area under amorphous peaks. The $\sum A_C$ and $\sum A_A$ values were determined from total area under crystal and amorphous peaks, respectively, of XRD pattern. It was found that the crystallinity (X_C) for the samples is increased from 85.3% to 94.4%, while the amorphous ratio (X_A) is decreased from 14.7% to 5.6%. The lattice parameters of the samples with trigonal system were calculated to be a=10.693 Å and c=36.569 Å for 10 at% Li, and a=10.340 Å and c=39.103 Å for 20 at% Li. With the addition of Li, a is decreased by about 3%, and c is increased distinctly about 7%. The lattice parameters were changed with the lithium content. Additionally, these values are close to both literature standard values of $Ca_{10}Li(PO_4)_7$ (a=10.421 Å and c=37.388 Å) and values reported by Song et al. (a=10.403 Å and c=37.307 Å) [28].

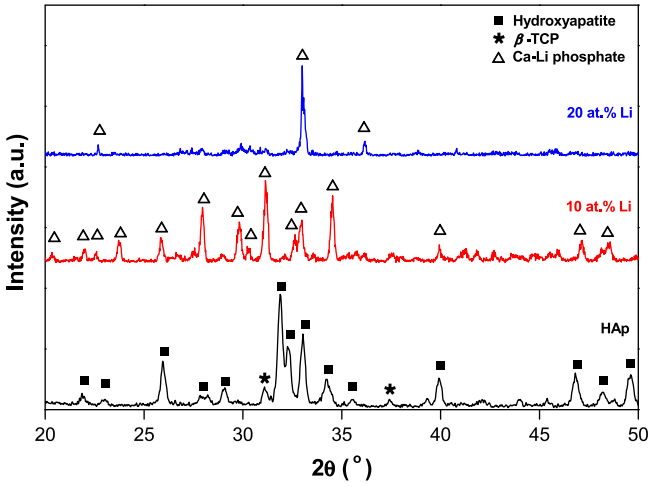

Fig. 1. XRD patterns of Ca–Li phosphate samples and hydroxyapatite.

Figs. 2 and 3 show DTA curves of the samples at different heating rates 5, 10, 15 and 20 °C min^{-1}. Tables 1 and 2 give the peak temperatures and enthalpy values of the samples for different heating rates. As seen in DTA curves of the samples, there is one peak in 10 at% Li, while there are two peaks in 20 at% Li. It is evaluated that the peak in the range of 840–800 °C is related to the crystallization of the samples. But, the first peak in 20 at% Li is due to the starting of crystallization. Two peaks correspond to the crystallization of lithium calcium phosphate. We used the peak in the range of 840–800 °C to evaluate the crystallization mechanism of the samples. For this, the equations of non-isothermal kinetics were used. According to the Johnson–Mehl–Avrami (JMA) theory, the activation energy (E_a) values of the samples can be calculated by the following Kissinger [29], Ozawa [30] and Boswell [31] equations, respectively:

$$Y = ln\left(\frac{\beta}{T_P^2}\right) = -\frac{E_a}{RT_P} + ln\left(\frac{k_o R}{E_a}\right) \quad (4)$$

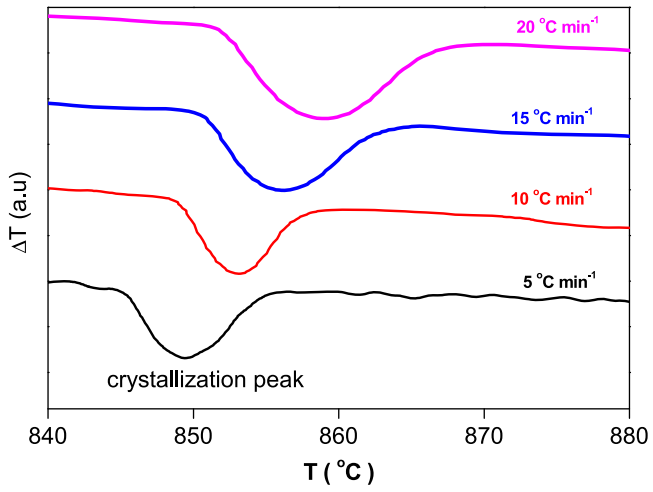

Fig. 2. DTA plots of 10 at% Li sample at different heating rates.

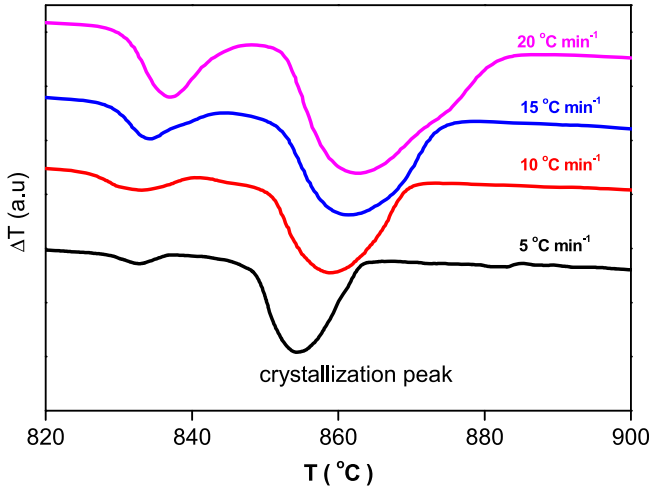

Fig. 3. DTA plots of 20 at% Li sample at different heating rates.

$$Y = ln\beta = -\frac{E_a}{RT_P} + C_1 \quad (5)$$

$$Y = ln\left(\frac{\beta}{T_P}\right) = -\frac{E_a}{RT_P} + C_2 \quad (6)$$

where β is the heating rate, R is the universal gas constant, T_p is the temperature at maximum peak, k_o is the pre-exponential frequency factor and C_1 and C_2 are the constants. The activation energies for the samples were calculated from the slopes of $ln(\beta/T_P^2)$ vs. $1/T_P$, $ln\beta$ vs. $1/T_P$ and $ln(\beta/T_p)$ plots shown in Figs. 4 and 5. According to the Kissinger equation, k_o can be determined by the intercept of $ln(\beta/T_P^2)$ vs. $1/T_P$ plot. Then, the crystallization rate (k) can be estimated by the

Table 1
DTA data for 10 at% Li sample at various heating rates.

α (°C min^{-1})	T_o (°C)	T_f (°C)	T_p (°C)	ΔH (J g^{-1})
5	845.45	854.24	849.47	−20.95
10	849.05	857.12	853.06	−18.64
15	850.89	862.38	856.15	−19.24
20	852.06	866.12	858.86	−17.21

Table 2
DTA data for 20 at% Li sample at various heating rates.

	First peak				Second peak			
α (°C min^{-1})	T_o (°C)	T_f (°C)	T_p (°C)	ΔH (J g^{-1})	T_o (°C)	T_f (°C)	T_p (°C)	ΔH (J g^{-1})
5	828.59	836.28	832.80	−2.08	848.66	862.81	854.33	−34.49
10	826.60	841.20	833.00	−3.67	851.01	869.06	858.81	−32.34
15	828.87	842.21	834.19	−6.58	851.82	873.17	861.40	−36.60
20	831.02	843.68	837.29	−9.39	853.08	881.36	862.68	−42.76

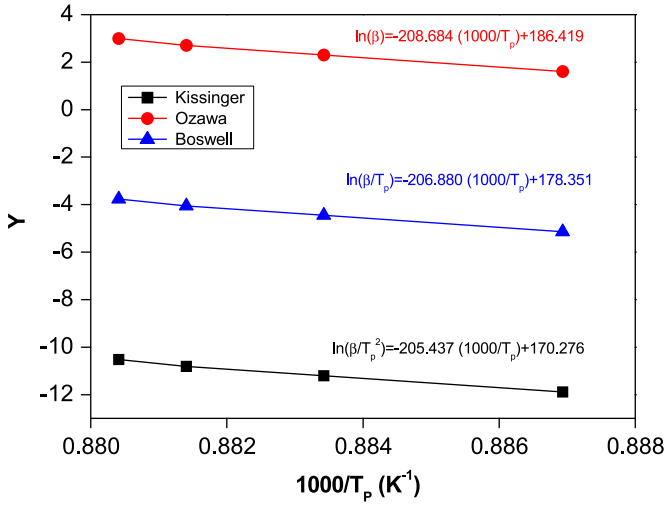

Fig. 4. Kissinger, Ozawa and Boswell plots of 10 at% Li ceramic.

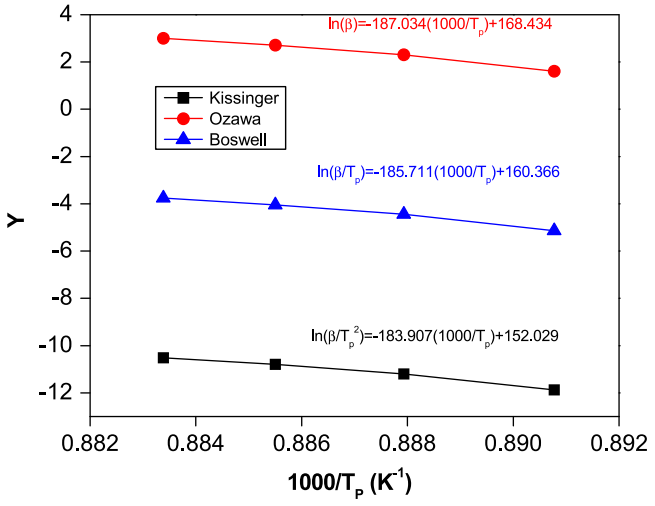

Fig. 5. Kissinger, Ozawa and Boswell plots of 20 at% Li ceramic.

following Arrhenius equation [32]:

$$k = k_o \, exp\left(-\frac{E_a}{RT_P}\right) \tag{7}$$

The Avrami exponent (n) can be estimated using the Augis–Bennet equation [33]

$$n = \frac{2.5}{\Delta\tau_{FWHM}} \frac{RT_P^2}{E_a} \tag{8}$$

where $\Delta\tau_{FWHM}$ is the width of the exothermic peak at the half maximum intensity. The calculated values of the parameters, containing the rate constant, pre-exponential frequency factor, Avrami exponent and activation energy, are summarized in Table 3. As seen in Tables 1–3, the activation energy and enthalpy values of the ceramics are increased with the addition of Li. The activation energy of 10 at% Li calcium phosphate ceramic is higher than that of 20 at% Li calcium phosphate ceramic. This confirms that the crystallization of 10 at% Li calcium phosphate ceramic is easier than that of 20 at% Li calcium phosphate ceramic.

The value of the pre-exponential frequency factor sharply decreases with increasing amount of lithium. The average values of the Avrami exponent are nearly 1, and this result suggests that both the samples have the surface nucleation and one-dimensional growth [34]. The mean values of the rate constant are 1.61 and 6.46 s^{-1} for 10 at% Li and 20 at% Li, respectively. k value is four times increased with the addition of Li. This result implies that the crystallization is increased with the amount of lithium.

FTIR spectra of these samples are illustrated in Fig. 6. The bands belonging to the stretching and bending modes of phosphate groups were observed in the range of 1200–550 cm^{-1} [35]. The bands at 3421 and 1614 cm^{-1} are originated from adsorbed water [36]. Although the sharpness of the peaks changed with the addition of Li, there is no shift in the peak positions. Moreover, any peak belonging to the carbonate group, which is a common impurity in both natural and synthetic hydroxyapatite, was not detected [37,38].

Table 3
The values calculated from non-isothermal crystallization kinetics.

Sample	α (°C min^{-1})	k (s^{-1})	k_o (s^{-1})	n	E_a Kissinger (kJ mol^{-1})	E_a Ozawa (kJ mol^{-1})	E_a Boswell (kJ mol^{-1})
10% Li	5	0.63	1.83×10^{79}	1.65	1708	1735	1720
	10	1.12		1.19			
	15	1.84		1.03			
	20	2.85		0.83			
20% Li	5	2.87	1.95×10^{71}	1.83	1529	1555	1544
	10	5.48		1.38			
	15	7.94		1.14			
	20	9.53		0.92			

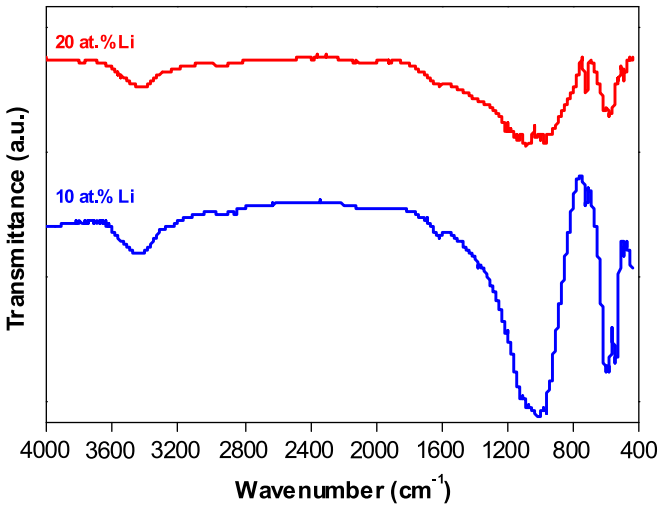

Fig. 6. FTIR plots of the samples.

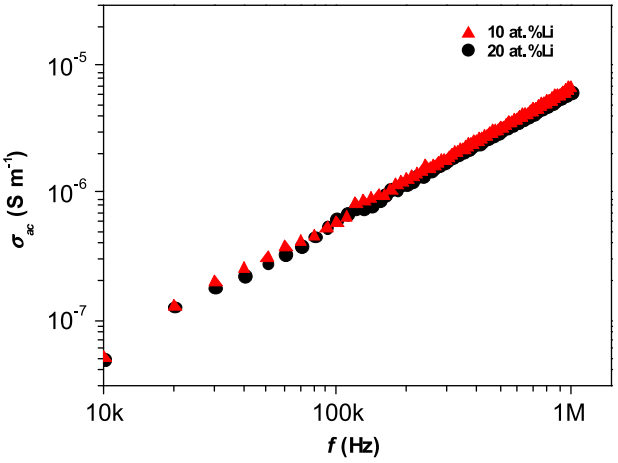

Fig. 7. Plots of σ_{ac} vs. f for the samples.

Fig. 7 shows the plot of the alternating current conductivity (σ_{ac}), which was calculated from the measured impedance values vs. frequency, and its dependence on frequency can be

expressed as the following relation [39]:

$$\sigma_{ac} = \sigma_{dc} + B\omega^{s} \tag{9}$$

where σ_{dc} is the direct current conductivity, B is a constant, ω is the angular frequency and s is an exponent. The ac conductivity mechanism was analyzed by Eq. (6) and the s value was calculated from the slope of log σ_{ac} vs. log f curve for each sample [40]. The calculated values of s are 1.018 and 1.024 for 10 at% Li and 20 at% Li, respectively, and these are almost equal to 1. This result implies that the hopping motion involves a translational motion with a sudden hopping [41]. Additionally, all the samples exhibit the insulator behavior, due to their high electrical resistances about $10^{12}\,\Omega$ [42]. In addition, there is no measurable direct current conductivity (σ_{dc}) of all ceramic samples; the s value is close to 1 [43].

The dielectric constant of the ceramic samples was calculated by the following equation:

$$\varepsilon' = \frac{C_p t}{\varepsilon_o A} \tag{10}$$

where ε' is the dielectric constant, C_p is the parallel capacitance, t is the thickness of the sample, ε_o is the permittivity of vacuum (8.85×10^{-12} F m^{-1}) and A is the area of cross-section of the sample [44]. Fig. 8 shows the plot of dielectric constant of as-prepared samples vs. frequency with error bars. The calculated values of ε' at 1 kHz are 11.18 and 10.00, for 10 at% Li and 20 at % Li, respectively. As can be seen in Fig. 8, the value of ε' shows a small increase with increasing amount of Li. All the ε' values are in the range of 10–12, approximately. The dielectric constants of Li doped HAp are much lower than those of Zn and Mg doped HAp [18,44]. This difference is due to the high dielectric polarization ability of the samples with Li content with respect to Zn and Mg doped HAp samples. Also, ionic substitution of Li in the apatite structure increases the dielectrical polarization and in turn, $Ca_{10}Li(PO_4)_7$ ceramics exhibit low dielectric constant. It is evaluated that the change in dielectric constant of the samples makes a contribution to healing in bone fractures due to the spreading of electromagnetic fields in bone fractures. Thus, the Li doped HAp of low dielectric constant can have an advantage for healing in bone fractures.

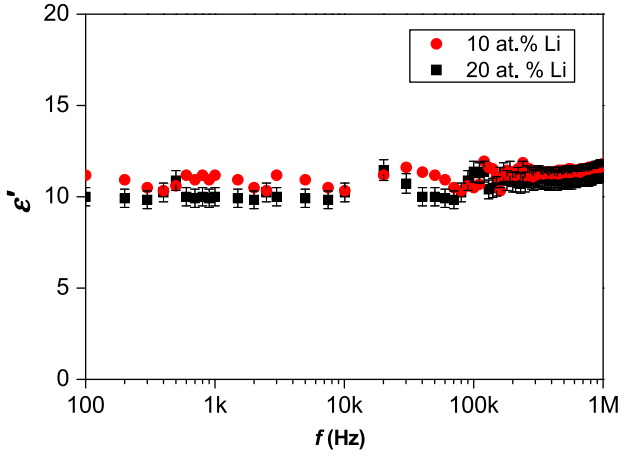

Fig. 8. Plots of ε' vs. f for the samples.

The density (ρ) of the samples was calculated using the Archimedes method [45]

$$\rho = \frac{W_a}{W_a - W_b}\rho_\ell \tag{11}$$

where W_a and W_b are weights of the sample in air and liquid, respectively. ρ_ℓ is the density of the immersion liquid. Distilled water was used as the immersion liquid. The calculated density values of the samples were found to be 3340 and 2630 kg m^{-3} for 10 at% Li and 20 at% Li, respectively. The density considerably decreases with the increase of Li concentration in calcium lithium phosphate. As is known, the theoretical value of density of Li at 25 °C is 534 kg m^{-3} [46]. Hence, a decrease in the density of sample with increasing amount of lithium is expected. The change in density can be associated with the ionic substitutions originated from lithium in the apatite structure [47], because both the ionic radius and the density of lithium are very small, in comparison to those of calcium [48].

Scanning electron microscope (SEM) pictures and electron dispersive X-ray (EDX) analysis results of the 10 at% Li and 20 at% Li are shown in Figs. 9 and 10, respectively. While the 10 at% Li sample has a fibrous structure similar to those of bone and synthetic HAp, the 20 at% Li sample has non-fibrous structure.

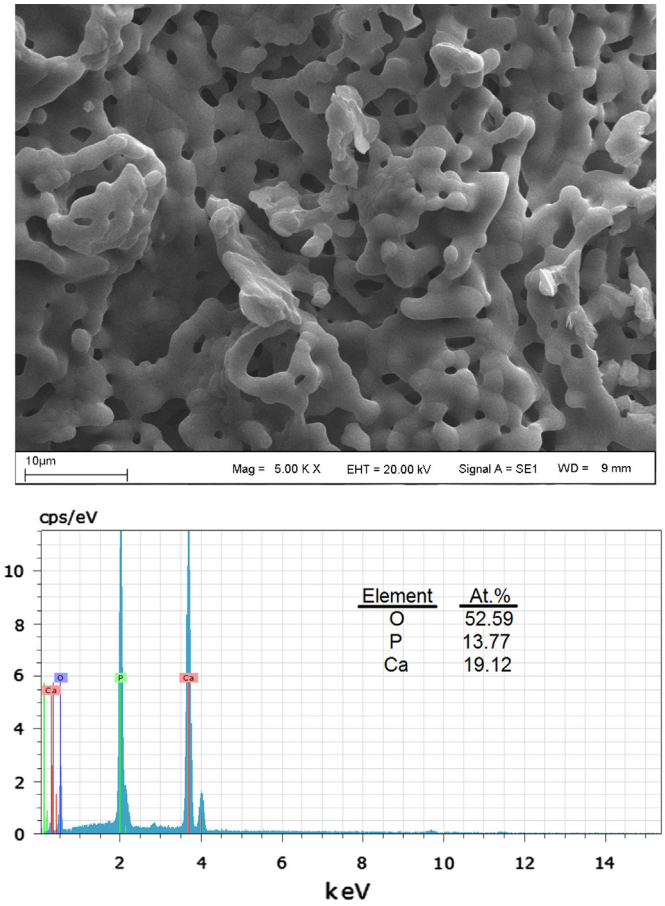

Fig. 9. SEM picture and EDX analysis result of 10 at% Li sample.

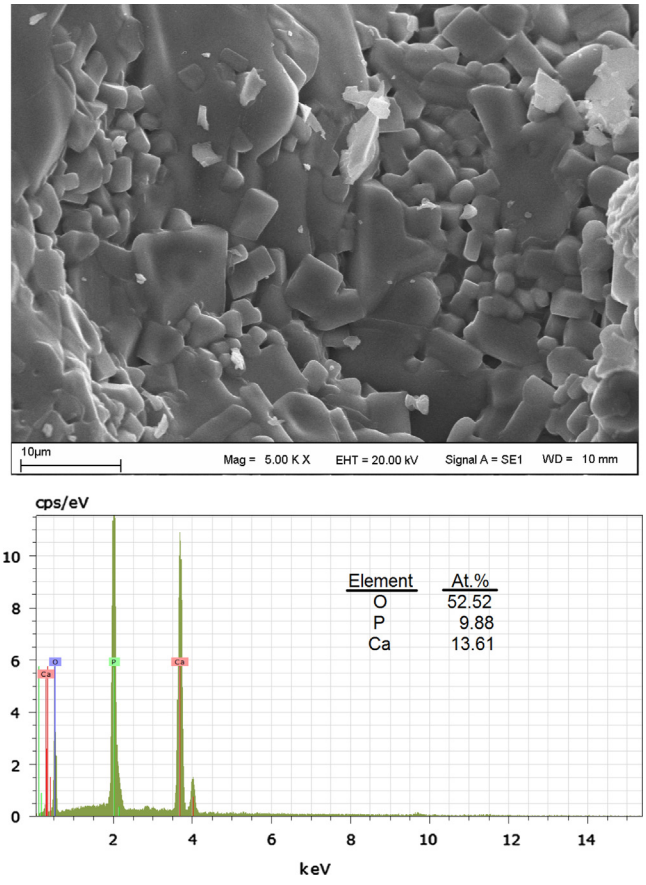

Fig. 10. SEM picture and EDX analysis result of 20 at% Li sample.

The stoichiometric ratio of Ca/P is calculated to be 1.39 and 1.38 for 10 at% Li and 20 at% Li, respectively, and this is due to Ca-deficiency. Lithium cannot be detected by EDX. For 10 at% Li sample, the size of grains appears in the range of 1–5 µm, and most of them are about 3 µm. The distribution of size of grains for 20 at% Li sample is in the range of 1–25 µm, and most of them are about 5 µm.

4. Conclusions

The $Ca_{10}Li(PO_4)_7$ samples were synthesized by the sol–gel method. The crystallite size and crystallinity are increased with increasing amount of lithium. The crystal structure of HAp is transformed from hexagonal to trigonal with the addition of Li. The apatitic structure belonging to HAp was transformed fully to $Ca_{10}Li(PO_4)_7$ phase. The activation energy and pre-exponential frequency factor significantly decrease with the addition of Li. Both the samples possess surface nucleation and one-dimensional growth since the average values of the Avrami exponent are almost equal to 1. The rate constant increases four times with the addition of Li. The alternating current conductivity increases with increasing frequency. The dielectric constant of the samples was found to be in the range of 10–12. The structural properties of the HAp changed with the addition of lithium.

Acknowledgments

This work was supported by Management Unit of Scientific Research projects of Firat University (FÜBAP) (Project Number: FF.12.31).

References

[1] L.L. Hench, Sol–gel materials for bioceramic applications, Current Opinion in Solid State and Materials Science 2 (1997) 604–610.
[2] S.V. Dorozhkin, Bioceramics of calcium orthophosphates, Biomaterials 31 (2010) 1465–1485.
[3] J. Park, Bioceramics: Properties, Characterizations, and Applications, Springer, New York, 2008.
[4] M. Manzano, M. Vallet-Regí, Revisiting bioceramics: Bone regenerative and local drug delivery systems, Progress in Solid State Chemistry 40 (2012) 17–30.
[5] A. Bigi, E. Boanini, C. Capuccini, M. Gazzano, Strontium-substituted hydroxyapatite nanocrystals, Inorganica Chimica Acta 360 (2007) 1009–1016.
[6] Z. Zhang, H. Yamamoto, M. Aizawa, Synthesis of plate-shaped hydroxyapatite via an enzyme reaction of urea with urease and its characterization, Powder Technology 222 (2012) 193–200.
[7] D.S. Seo, J.K. Lee, Dissolution of human teeth-derived hydroxyapatite, Annals of Biomedical Engineering 36 (2008) 132–140.
[8] T.S.B. Narasaraju, D.E. Phebe, Some physico-chemical aspects of hydroxylapatite, Journal of Materials Science 31 (1996) 1–21.
[9] Z. Zou, K. Lin, L. Chen, J. Chang, Ultrafast synthesis and characterization of carbonated hydroxyapatite nanopowders via sonochemistry-assisted microwave process, Ultrasonics Sonochemistry 19 (2012) 1174–1179.
[10] Y. Zhang, Y. Yokogawa, X. Feng, Y. Tao, Y. Li, Preparation and properties of bimodal porous apatite ceramics through slip casting using different hydroxyapatite powders, Ceramics International 36 (2010) 107–113.
[11] L.L. Hench, Bioceramics: from concept to clinic, Journal of the American Ceramic Society 74 (1991) 1487–1510.
[12] C. Li, Crystalline behaviors of hydroxyapatite in the neutralized reaction with different citrate additions, Powder Technology 192 (2009) 1–5.
[13] H. Zhou, J. Lee, Nanoscale hydroxyapatite particles for bone tissue engineering, Acta Biomaterialia 7 (2011) 2769–2781.
[14] D.G. Wang, C.Z. Chen, J. Ma, T. He, Microstructure evolution of sol–gel HAp films, Applied Surface Science 257 (2011) 2592–2598.
[15] P. Kanchana, C. Sekar, Influence of sodium fluoride on the synthesis of hydroxyapatite by gel method, Journal of Crystal Growth 312 (2010) 808–816.
[16] A.R. Kumar, S. Kalainathan, Sol–gel synthesis of nanostructured hydroxyapatite powder in presence of polyethylene glycol, Physica B 405 (2010) 2799–2802.
[17] C.C. Silva, Estudo das Propriedades Ópticas, Elétricas e Térmicas da Hidroxiapatita obtida por Moagem de Alta Energia, seus Compósitos e Filmes Espessos, Ph.D. Thesis, Universidade Federal do Ceará, Brasil, 2003.
[18] O. Kaygili, C. Tatar, The investigation of some physical properties and microstructure of Zn-doped hydroxyapatite bioceramics prepared by sol–gel method, Journal of Sol–Gel Science and Technology 61 (2012) 296–309.
[19] M.A. Fanovich, M.S. Castro, J.M. Porto López, Analysis of the microstructural evolution in hydroxyapatite ceramics by electrical characterisation, Ceramics International 25 (1999) 517–522.
[20] S. Ramaprasad, Magnetic resonance spectroscopic imaging studies of lithium, Progress in Nuclear Magnetic Resonance Spectroscopy 47 (2005) 111–121.
[21] D. Focosi, A. Azzará, R.E. Kast, G. Carulli, M. Petrini, Lithium and hematology: established and proposed uses, Journal of Leukocyte Biology 85 (2009) 20–28.

[22] M. Petrini, A Azzará, Lithium in the treatment of neutropenia, Current Opinion in Hematology 19 (2012) 52–57.
[23] A. Zamani, G.R. Omrani, M.M. Nasab, Lithium's effect on bone mineral density, Bone 44 (2009) 331–334.
[24] A.S. Rao, N. Kremenevskaja, J. Resch, G. Brabant, Lithium stimulates proliferation in cultured thyrocytes by activating Wnt/β-catenin signalling, European Journal of Endocrinology 153 (2005) 929–938.
[25] H.R. Li, C.Q. Qin, Z.H. Zhang, J.C. Zhu, Y. Liu, Stimulation effect of lithium on the metabolic activity of liver tissue mitochondria measured by microcalorimetry, Biological Trace Element Research 114 (2006) 163–173.
[26] B.D. Cullity, Elements of X-ray Diffraction, Addison-Wesley Publishing Company, Massachussets, 1978.
[27] G.K. Williamson, W.H. Hall, X-ray line broadening from filed aluminium and wolfram, Acta. Metallurgica 1 (1953) 22–31.
[28] E. Song, Z. Weiren, G. Zhou, X. Dou, C. Yi, M. Zhou, Luminescence properties of red phosphors $Ca_{10}Li(PO_4)_7$:Eu^3, Journal of Rare Earths 29 (2011) 440–443.
[29] H.E. Kissinger, Reaction kinetics in differential thermal analysis, Analytical Chemistry 29 (1957) 1702–1706.
[30] T. Ozawa, Estimation of activation energy by isoconversion methods, Thermochimica Acta 203 (1992) 159–165.
[31] P.G. Boswell, On the calculation of activation energies using a modified Kissinger method, Journal of Thermal Analysis 18 (1980) 353–358.
[32] C. Dohare, N. Mehta, A. Kumar, Effect of some metallic additives (Ag, Cd, and Zn) on the crystallization kinetics of glassy $Se_{70}Te_{30}$ alloy, Materials Chemistry and Physics 127 (2011) 208–213.
[33] J. Ma, C.Z. Chen, D.G. Wang, J.H. Hu, Synthesis, characterization and in vitro bioactivity of magnesium-doped sol–gel glass and glass-ceramics, Ceramics International 37 (2011) 1637–1644.
[34] N. Gupta, A. Dalvi, S. Bhardwaj, A.M. Awasthi, Crystallization and glass transition kinetics in Cu^+ ion substituted Cu_x–Ag_{1-x}–I–Ag_2O–V_2O_5 superionic glasses, Journal of Non-Crystalline Solids 357 (2011) 1811–1815.
[35] S. Koutsopoulos, Synthesis and characterization of hydroxyapatite crystals: a review study on the analytical methods, Journal of Biomedical Materials Research 62 (2002) 600–612.
[36] W. Wei, X. Zhang, J. Cui, Z. Wei, Interaction between low molecular weight organic acids and hydroxyapatite with different degrees of crystallinity, Colloids and Surfaces A 392 (2011) 67–75.
[37] M. Markovic, B.O. Fowler, M.S. Tung, Preparation and comprehensive characterization of a calcium hydroxyapatite reference material, Journal of Research of the National Institute of Standards and Technology 109 (2004) 553–568.
[38] M. Jevtič, M. Mitrič, S. Škapin, B. Jančar, N. Ignjatovič, D. Uskokovič, Crystal structure of hydroxyapatite nanorods synthesized by sonochemical homogeneous precipitation, Crystal Growth and Design 8 (2008) 2217–2222.
[39] M. Pollak, T.H. Geballe, Low-frequency conductivity due to hopping processes in silicon, Physical Review 22 (1961) 1742–1753.
[40] H. Jain, S. Krishnaswami, Composition dependence of frequency power law of ionic conductivity of glasses, Solid State Ionics 105 (1998) 129–137.
[41] K. Funke, Jump relaxation in solid electrolytes, Progress in Solid State Chemistry 22 (1993) 111–195.
[42] T.T. Davis, A. Vatave, J. Patla, J. Bernbeck, B.R. Delamarter, H.W. Bae, Pedicle screw electrical resistance: hydroxyapatite coated versus non-coated, Poster Presentation, American Association of Neurological Surgeons, Orlando, Florida, USA, February 17–20, 2010.
[43] R.M.P. Colloquia, Universality of ac conduction in disordered solids, Reviews of Modern Physics 72 (2000) 873–892.
[44] O. Kaygili, C. Tatar, F. Yakuphanoglu, Structural and dielectrical properties of Mg_3–$Ca_3(PO_4)_2$ bioceramics obtained from hydroxyapatite by sol–gel method, Ceramics International 38 (2012) 5713–5722.
[45] O. Kaygili, H. Yavuz, The effects of gamma irradiation on non-isothermal crystallization kinetics and microhardness of the Li_2O–Al_2O_3–SiO_2 glass–ceramic, Journal of Thermal Analysis and Calorimetry 102 (2010) 681–684.
[46] F. Cardarelli, in: Materials Handbook: A Concise Desktop Reference, second ed., Springer-Verlag, London, 2008.
[47] E. Landi, G. Logroscino, L. Proietti, A. Tampieri, M. Sandri, S. Sprio, Biomimetic Mg-substituted hydroxyapatite: from synthesis to in vivo behaviour, Journal of Materials Science: Materials in Medicine 19 (2008) 239–247.
[48] R.D. Shannon, Revised effective ionic radii and systematic studies of interatomic distances in halides and chalcogenides, Acta Crystallographica 32 (1976) 751–767.